Journal of Atmospheric and Solar–Terrestrial Physics 154 (2017) 167–179

Contents lists available at ScienceDirect

Journal of Atmospheric and Solar–Terrestrial Physics

journal homepage: www.elsevier.com/locate/jastp

Thermospheric density estimation and responses to the March 2013 geomagnetic storm from GRACE GPS-determined precise orbits

Andres Calabia[a,b], Shuanggen Jin[a,c,*]

[a] Shanghai Astronomical Observatory, Chinese Academy of Sciences, Shanghai 200030, China
[b] University of Chinese Academy of Sciences, Beijing 100049, China
[c] Department of Geomatics Engineering, Bulent Ecevit University, Zonguldak 67100, Turkey

ARTICLE INFO

Keywords:
Non-gravitational accelerations
Atmospheric density
GRACE
Precise orbit ephemeris (POE)

ABSTRACT

The thermospheric mass density variations and the thermosphere-ionosphere coupling during geomagnetic storms are not clear due to lack of observables and large uncertainty in the models. Although accelerometers on-board Low-Orbit-Earth (LEO) satellites can measure non-gravitational accelerations and derive thermospheric mass density variations with unprecedented details, their measurements are not always available (e.g., for the March 2013 geomagnetic storm). In order to cover accelerometer data gaps of Gravity Recovery and Climate Experiment (GRACE), we estimate thermospheric mass densities from numerical derivation of GRACE determined precise orbit ephemeris (POE) for the period 2011–2016. Our results show good correlation with accelerometer-based mass densities, and a better estimation than the NRLMSISE00 empirical model. Furthermore, we statistically analyze the differences to accelerometer-based densities, and study the March 2013 geomagnetic storm response. The thermospheric density enhancements at the polar regions on 17 March 2013 are clearly represented by POE-based measurements. Although our results show density variations better correlate with *Dst* and k-derived geomagnetic indices, the auroral electroject activity index *AE* as well as the merging electric field E_m picture better agreement at high latitude for the March 2013 geomagnetic storm. On the other side, low-latitude variations are better represented with the *Dst* index. With the increasing resolution and accuracy of Precise Orbit Determination (POD) products and LEO satellites, the straightforward technique of determining non-gravitational accelerations and thermospheric mass densities through numerical differentiation of POE promises potentially good applications for the upper atmosphere research community.

1. Introduction

Within the process of deriving precise ephemeris from GPS observations, the reduced-dynamic POD approach in Low-Orbit-Earth (LEO) is one of the most accurate strategies (Wu et al., 1991). High-precision GPS orbit determination is sensitive to geometrical GPS factors (e.g., dilution of precision), and the combination with the dynamical models (e.g., atmospheric drag) and GPS measurement errors. In the last half century, thermospheric mass density variations, anomalies and climatology have been investigated and reported (Qian and Solomon, 2012). However, the functional dependencies of all geophysical processes in the ionosphere-thermosphere system are still unclear (Ridley et al., 2006; Jin et al., 2013), and the current thermospheric mass density models are incapable to predict the variability as accurately and efficiently required in POD.

Besides pressure gauge and mass spectrometer measurements, the analysis of satellite orbital decay through the perturbation equations has been the basis to derive thermospheric mass densities since 1958 (Priester et al., 1967). Currently, accelerometers on LEO satellites are being used to measure non-gravitational accelerations from which the mass density can be deduced with unprecedented precision (e.g., Bruinsma et al., 2004; Sutton, 2008; Doornbos, 2011). Unfortunately, not all the LEO satellites carry these precious accelerometers and carrying ones can be affected by instrument malfunction, data loss and other external factors. For instance, the twin satellites of Gravity Recovery and Climate Experiment (GRACE, Tapley et al., 2004) carry high precision electrostatic accelerometers to separate non-gravitational from gravitational forces. Since solar energy is the basis of the instrument powering, the modus operandi is strongly dependent on battery-load and eclipse conditions. GRACE's orbit plane precesses relative to the Sun every 161 days, and the use of battery or solar panels depends on the β' angle (angle between the orbit plane and the Earth-Sun line). For large β' angles, the satellite operates only from its solar array power, but for small β' angles, the satellite

* Corresponding author.
E-mail address: sgjin@shao.ac.cn (S. Jin).

http://dx.doi.org/10.1016/j.jastp.2016.12.011
Received 6 October 2016; Received in revised form 23 November 2016; Accepted 24 December 2016
Available online 28 December 2016
1364-6826/

operates partly from the solar panels, and partly from the battery. Unfortunately, the mission status strongly depends on the battery health, and after 9 year of continuous operability, its performance has obliged to conduct a power-supply strategy. That is to say, the accelerometers have been turned off, during intermittent periods of approximately one month, to reduce the power requirements. The first long-term issue occurred on 28 December 2010, when the accelerometer on-board the GRACE-B satellite was turned off until 7 February 2011. The following periods ensued on January, June and November of 2011, May and October of 2012, March and August of 2013, July and December of 2014, and May/June of 2015. Currently, the accelerometers and the microwave assembly have been turned off since September 2015, but the GPS and star camera data are being collected. Thus, since no atmospheric densities can be derived during these periods, a technique to derive non-gravitational accelerations from POD products can be the key when accelerometer measurements are not available.

In the recent years, several studies have shown that non-gravitational accelerations can be estimated through GPS-based reduced-dynamic POD of LEO. For instance, van den IJssel and Visser (2007, 2010) estimated non-gravitational accelerations by omitting the non-gravitational force models in a highly-reduced dynamic POD process, and assessed the method through various simulated scenarios based on the GRACE mission. In their scheme, the GEODYN software is employed for all POD computations, which are based in a standard Bayesian weighted batch least-squares estimator. The piecewise linear functions are used to be computed at 10–15 min resolution for best results. In order to avoid a possible degraded quality at the edges, the orbits are processed in 30 h batches, with 3–6 h overlaps between subsequent orbits. Recent results using this technique for different missions can be found in van den IJssel (2014), Siemes et al. (2016), and Doornbos et al. (2014). Unfortunately, a unique solution in each interval of estimated non-gravitational accelerations allows no high-frequency variations caused by, e.g., geomagnetic storms, and no meaningful solution can be obtained in the radial direction.

In the POD process, atmospheric densities can also be obtained as a correction to an atmospheric model. For instance, McLaughlin et al. (2013) used a set of POE in a sequential orbit determination scheme to estimate thermospheric densities from GRACE, CHAMP, and TerraSAR-X. Using the Orbit Determination Tool Kit (ODTK), the authors input the POE in a sequential processing, filtering and smoothing scheme to obtain the time variable densities and ballistic coefficients. The ODTK software package uses the technique developed by Wright (2003) for density and ballistic coefficient estimation. In McLaughlin et al. (2013), comparisons with CHAMP and GRACE accelerometer measurements showed that POE-based densities are more accurate than the densities estimated from commonly used empirical models. This is a clear example showing that non-gravitational accelerations can be derived from GNSS measurements when accelerometers are not available (e.g., TerraSAR-X). By applying all best available force models in multiple LEO, Kuang et al. (2014) have recently computed non-gravitational accelerations and inferred thermospheric mass densities by estimating the stochastic accelerations that compensate for the dynamic model errors in the reduced-dynamic POD approach. In this method, daily solutions were generated using orbit arcs of 30 h, with stochastic accelerations estimated from GPS ionosphere-free carrier phase and carrier-smoothed pseudo-range measurements. Contrasting the technique of Kuang et al. (2014) with the technique of van den IJssel and Visser (2007, 2010), both accuracy and resolution were improved because estimating accelerations to compensate for the model errors (smaller estimations) allows stronger stochastic constraints in the reduced-dynamic filtering. Through the error analysis of several LEO satellites, the authors identified useful data from CHAMP, GRACE-A/B, TerraSAR-X, and SAC-C. Using this technique at 5 min interval, density estimates showed useful information up to altitude as high as 715 km (at higher altitudes, errors in the measurements overcome the actual density).

Although the above studies have proven successfully results in retrieving thermospheric densities from GNSS observables, the use of POD least-squares estimators to derive additional measurements can become a complex task, and recent studies have shown that non-gravitational accelerations can be derived from the numerical differentiation of reduced-dynamic precise orbit velocities (Calabia and Jin, 2015). With the increasing number of LEO satellites being equipped with a high-precision GPS receivers, and more enhanced data processing and orbit determination strategies, the straightforward technique of determining satellite accelerations through numerical differentiation promises potentially good applications. In the reduced-dynamic POD, the errors induced by imperfections in the force-models are mitigated by the high accuracy of GPS observations, and the error committed when deriving total accelerations from numerical differentiation has shown to be acceptable for accelerometer calibration. For instance in Calabia et al. (2015), the numerical differentiation of reduced-dynamic precise orbit velocities provided comparable results for accelerometer calibration than that given by the second numerical derivative of kinematic positions of Bezděk (2010) and the POD strategy of Bruinsma et al. (2004). In addition, Calabia and Jin (2016a) conducted a further study on the differences between the numerical derivative and the accelerometer readouts (only the radial direction was investigated). In this paper, we employ numerically differentiated GRACE's precise orbit ephemeris (POE) to derive and investigate thermospheric mass density variations during 2011–2016. In addition, we statistically investigate the differences to accelerometer measurements for the assessment of the retrieval error (along-track direction).

During the last decade, considerable improvements have been achieved in observing and modeling thermospheric mass density responses to geomagnetic storms. For instance, Liu and Lühr (2005) and Sutton et al. (2005) investigated the severe geomagnetic storm of November 2003 from CHAMP (Challenging Minisatellite Payload) accelerometer measurements. Later, Bruinsma et al. (2006) included the GRACE measurements to study the same storm. Their results showed density increments up to 800%, a negligible time delay at high latitudes, and about a 4h delay at the equator. Then, Sutton et al. (2009) studied the thermospheric response to variations produced by the July 2004 geomagnetic storm from CHAMP accelerometer measurements. The resulting thermospheric time response was significantly shorter than those from the empirical models. Liu et al. (2010, 2011) modeled the dependence of density on the solar wind E_m, from CHAMP and GRACE accelerometers and, recently, Lu et al. (2014) have presented a case study of the April 2010 geomagnetic storm using multi-satellite accelerometer measurements and numerical simulations. However, during the 17 March 2013 geomagnetic storm (and for other many interesting periods), accelerometer measurements onboard GRACE satellites are not available. This study aims to estimate and monitor understand thermospheric mass density variations during the March 2013 geomagnetic storm from numerical differentiation of determined GRACE POE.

2. Data and methods

In this section a brief introduction of the observational data is presented as well as the method to derive thermospheric mass densities from non-gravitational accelerations. Both accelerometer-based and POE-based densities are computed to be later compared employing statistical methods.

2.1. Observations and models

GRACE's Level 1B format record files can be downloaded from the Information System and Data Center (ISDC) GeoForschungsZentrum (GFZ) website (http://isdc.gfz-potsdam.de/). The highly sensitive tri-axial accelerometers on-board GRACE are used to measure the non-

gravitational acceleration acting on the satellites. Plus and minus drive voltages are applied to electrodes with respect to opposite sides of a proof-mass, whose electrical potential is maintained at a *dc* biasing voltage. Unfortunately, this *dc* level is the source of bias and bias fluctuations which must be corrected, e.g., using the parameterizations of Calabia et al. (2015). GRACE's star cameras provide the precise attitude references to determine the satellite's absolute orientation with respect to the International Celestial Reference System (ICRS). Precise orbit ephemeris (position and velocity) are generated by processing 5-minute GPS tracking data, through reduced-dynamic POD with stochastic acceleration estimated every 5-minute (Bertiger et al., 2002). Precise orbit ephemeris, thruster activation times, and satellite mass records are also included within the record files.

NRLMSISE-00 is an empirical global model of the Earth's atmosphere, which shows general mean variations of the atmospheric mass density (Picone et al., 2002). Its primary use is to aid predictions of satellite orbital decay due to atmospheric drag, and to know the average behaviors of thermospheric mass density variations. The earlier models MSIS-86 and MSISE-90 are based on Mass Spectrometer and Incoherent Scatter Radar measurements, and the current model has been updated with orbital drag and satellite accelerometer data (more details about expanded database can be found in Picone et al. (2002).

2.2. Data processing

In this study, we employ the method of Calabia and Jin (2015) and Calabia et al. (2015) to derive POE-based non-gravitational accelerations. The procedure is based on subtracting modeled time-varying gravitational forces from precise orbit accelerations. Non-gravitational forces acting on a LEO satellite include atmospheric drag ($\boldsymbol{F_D}$), irradiative accelerations and thruster firings. Whilst thruster firings can be easily removed by using the activation records, irradiative accelerations comprise a more elaborated modeling. The three main sources of irradiative accelerations are the direct solar radiation pressure, the reflected solar radiation pressure, and the terrestrial infrared radiation. While the terrestrial infrared radiation (long-wave radiation) is almost independent from illumination conditions, the other two solar radiations (short-wave radiation) must account for the planetary eclipse ratio (Montenbruck and Gill, 2013).

On the satellite's surface, one part of the incoming radiation is absorbed, and the other is reflected diffusely and specularly. The following equation has been used to determine the entire resultant force on the satellite due to the solar radiation (Luthcke et al., 1997):

$$\boldsymbol{a}_{sr} = \sum_{i=1}^{n_p} -\frac{E_{sr}\, A_i \hat{\boldsymbol{n}}_i \cdot \hat{\boldsymbol{s}}_{sun}^{sat}}{mc}\left[2\left(\frac{c_{rd,i}}{3} + c_{rs,i}\hat{\boldsymbol{n}}_i \cdot \hat{\boldsymbol{s}}_{sun}^{sat}\right)\hat{\boldsymbol{n}}_i + (1 - c_{rs,i})\hat{\boldsymbol{s}}_{sun}^{sat}\right] \tag{1}$$

where n_p is the number of plates, A_i is the plate area, c is the speed of light, $c_{rd,i}$ is the coefficient of diffusive reflectivity, $c_{rs,i}$ is the coefficient of specular reflectivity, m is the satellite mass, $\hat{\boldsymbol{n}}_i$ is the unit plate normal, $\hat{\boldsymbol{s}}_{sun}^{sat}$ is the unit sun-satellite vector, and $E_{sr} = sh{\cdot}1366(1AU/s_{sun}^{sat})^2$ is the flux on the Earth's atmosphere (1366 W/m^2), corrected from the yearly period of the Earth's orbit eccentricity and from the planetary eclipse ratio sh. Since GRACE's panel properties (Bettadpur, 2012) provide the coefficients of reflectivity for both, the visible (VIS) and the infrared (IR) part of the electromagnetic spectrum, these have been weighted by the amount of solar flux given for each spectral window (43% for VIS, and 53% for IR). Furthermore, the Earth albedo has been computed in a similar way:

$$\boldsymbol{a}_{ea} = \sum_{i=1}^{n_p}\sum_{j=1}^{grid} -\frac{E_{ea,j}\, A_i \hat{\boldsymbol{n}}_i \cdot \hat{\boldsymbol{s}}_j^{sat}}{mc}\left[2\left(\frac{c_{rd,i}}{3} + c_{rs,i}\hat{\boldsymbol{n}}_i \cdot \hat{\boldsymbol{s}}_j^{sat}\right)\hat{\boldsymbol{n}}_i + (1 - c_{rs,i})\hat{\boldsymbol{s}}_j^{sat}\right] \tag{2}$$

where the parameter $E_{\mathrm{ea},j} = E_{ea}^{R} + E_{ea}^{IR}$ is composed of short-wave E_{ea}^{R} and long-wave E_{ea}^{IR} radiation. For the short-wave radiation, we have computed the Earth's reflected solar radiation at each satellite position employing the monthly averages of the Earth's reflectivity index σ, which is given in a time-series of grids by the Total Ozone Mapping Spectrometer (TOMS) project (http://disc.sci.gsfc.nasa.gov/acdisc/TOMS). The contribution of each cell j of TOMS has been computed as follows (Bhanderi, 2005):

$$E_{\mathrm{ea,j}}^{\mathrm{R}} = f_j\, v_j\, E_{sr}\, \frac{A_j\, (\hat{\boldsymbol{n}}_j \cdot \hat{\boldsymbol{s}}_j^{sun})\, (\hat{\boldsymbol{n}}_j \cdot \hat{\boldsymbol{s}}_j^{sat})\, \sigma_j}{\pi\, |\hat{\boldsymbol{s}}_j^{sat}|^2} \tag{3}$$

where f_j and v_j are the field of views of the satellite and the sunlight function, A_j is the area of each cell j. The reflection angle on each cell is defined by the direction of the satellite $\hat{s}_j^{sat}$, the Sun $\hat{s}_j^{sun}$, and the cell normal-vector $\hat{\boldsymbol{n}}_j$. MATLAB-converted grids and useful codes can be found at http://www.bhanderi.dk/downloads/. The long-wave radiation has been modeled as a black body with a surface temperature of 288 °K (Earth), whose spectrum is mainly IR with an exitance of about 239 W/m^2 (Taylor, 2005). The IR irradiance $E_{\mathrm{ea},j}^{IR}$ from each visible cell of the Earth's surface has been computed as follows:

$$E_{\mathrm{ea,\,j}}^{\mathrm{IR}} = f_j\, 239\left(\frac{1AU}{s_{sun}^{j}}\right)^2 e_{IR,j}\, \frac{A_j\, \hat{\boldsymbol{n}}_j \cdot \hat{\boldsymbol{s}}_j^{sat}}{\pi\, |\hat{\boldsymbol{s}}_j^{sat}|^2} \tag{4}$$

where the Earth IR radiation $e_{IR,j}$ for each cell j is variable in latitude and the season (Knocke and Ries, 1987):

$$e_{IR} = e_0 + e_1 P_1 sin\varphi + e_2 P_2 sin\varphi$$

$$e_l = k_0 + k_1 cos\left[\omega(JD - t_0)\right] + k_2 sin\left[\omega(JD - t_0)\right] \tag{5}$$

where t_0 is the epoch of 22 December 1981, ω is the Earth orbit rotation rate around the Sun (2π/365.5), φ is the equatorial geocentric latitude, JD is the Julian Date, P_n is the Legendre polynomial of degree n, and e_0=0.68; e_2=−0.18; k_0=0; k_1=−0.07, and k_2=0.

After removing the irradiative effects from GRACE's non-gravitational accelerations, thermospheric mass densities have been derived using the drag-force formula:

$$\boldsymbol{F_D} = \frac{1}{2}\boldsymbol{C}A\rho v_r^2 \tag{6}$$

where $\boldsymbol{C}$ is the drag coefficient vector, A is the cross-sectional area perpendicular to $\boldsymbol{v_r}$, ρ is the atmospheric mass density, and $\boldsymbol{v_r} = -\dot{\boldsymbol{r}}_{sat} + \boldsymbol{v_c} + \boldsymbol{v_w}$ is the relative velocity of the atmosphere with respect to the spacecraft, which includes the co-rotating atmosphere $\boldsymbol{v_c}$ and the horizontal winds $\boldsymbol{v_w}$ (Doornbos, 2011). Horizontal wind velocities $\boldsymbol{v_w}$ have been computed from the horizontal wind model HWM07 (Drob et al., 2008), and the velocity of the co-rotating atmosphere $\boldsymbol{v_c}$ has been computed as the vector product between the Earth angular rotation and the satellite's position vector $\boldsymbol{r_{sat}}$. For the drag coefficient vector $\boldsymbol{C}$, we employ the parameterizations given in Mehta et al. (2013). After solving the drag-force equation for the densities at each satellite position, the derived values have been normalized to a common height of 475 km, following the indications of Rentz and Lühr (2008):

$$\rho(\lambda, \phi, 475km, t) = \rho_{obs}(\lambda, \phi, h, t)\frac{\rho_{model}(\lambda, \phi, 475km, t)}{\rho_{model}(\lambda, \phi, h, t)} \tag{7}$$

where $\rho_{model}(\lambda, \varphi, h, t)$ are the densities computed from the NRMSISE00 empirical model, in geographical coordinates, and at the same positions and times as the measurements $\rho_{obs}(\lambda, \varphi, h, t)$. Since the GRACE orbit altitude varies from 500 km in 2003 to 440 km in 2015 (scale height of 60 km), the errors caused by the normalization are expected to be within 5%. See Bruinsma et al. (2006) for a detailed discussion on errors committed in density normalization.

2.3. Uncertainty analysis

The most important sources of error in accelerometer-based density retrieval are caused by the uncertainty in the drag coefficient and the errors in the horizontal wind model. Mehta et al. (2014) showed that using different gas-surface interaction models to estimate GRACE's drag coefficient can differs by ~15% during solar minimum conditions, and by ~2-3% during solar maximum. In this study we employ the physical drag coefficient given in Mehta et al. (2013), which under low solar activity levels, have shown to be more accurate than employing a constant energy accommodation coefficient and a flat plate model. On the other side, errors in GRACE's derived densities due to zonal and meridional winds are estimated at 1%, and 4% per 100 m/s, respectively (Bruinsma et al., 2006). Therefore, since the accuracy of accelerometer-based densities for low to moderate geomagnetic activity is estimated to be less than 10% (Bruinsma et al., 2006), the precision of the POE-density estimates can be assessed by comparison. In this scheme, the differences between accelerometer-based and POE-based densities can be statistically investigated to elucidate a reasonable magnitude of error in the POE-based densities.

In addition to the standard statistical methods (e.g., correlation coefficients, absolute error, standard deviation, etc.), the differences between accelerometer-based and POE-based densities can be investigated in space and time via the Principal Component Analysis (PCA). Previous studies have proven the suitability of this technique for the spatiotemporal data analysis of satellite measurements, e.g., Matsuo and Forbes (2010), Calabia and Jin (2016a, 2016b). Instead of estimating the principal components with a sequential nonlinear regression analysis of one-dimensional measurements along satellite tracks (Matsuo and Forbes, 2010), we examine in detail the covariance matrix of a grid time series (Calabia and Jin, 2016a). In this way, ascending and descending orbits first have been separated to derive a complete time series of grids. For the development in longitude, the values have been biased 360° after a grid (world-map) is completed. Taking into account time processing and required physical memory, we achieved an optimal resolution of 3° (world-map of 120x60 cells) using a standard desktop computer. Following to this approach, the variability of each grid is synthesized in two temporal dimensions: the latitudinal variation, defined by the half orbital period (3.99 min per westward degree), and the longitudinal variation, defined by the equatorial orbit shift (31.37 s per latitudinal degree). Then, the linear interpolation of measurements (as recommended by Calabia and Jin, 2016a), and the clipping of the resulting strip has been conducted (the trimming of each world-map is defined by the Earth revolution and the apsidal precession of GRACE, i.e. 23h 56min). Finally, the eigenvalue problem for the PCA has been solved employing the readily computable algorithm of Bjornsson and Venegas (1997). The method requires the use of a two-dimensional matrix where each row represents a given instant (or period) of time, and each column a time series for a given location. In this study, each grid has been expanded into one-dimensional array (120x60=7200), and a matrix of 7200x1831 cells has been created from the 1831 days to analyze (grids from 2011 to 2016, so each row corresponds to a single day). Note that each grid corresponds to 23h 56 min, so we obtain 5 grids extra in the period 2011–2016. The solution is a diagonal matrix containing the eigenvalues of the covariance matrix, and a matrix of the corresponding eigenvectors. Each eigenvector is a map, and the contribution to the total variability is given by its corresponding eigenvalue. Since all derived grids are equally affected by these longitudinal and latitudinal variations, the resulting PCA components follow the same pattern. More details about this technique can be found in Calabia and Jin (2016a).

2.4. Local Solar Time and annual variations

Previous to study short-term variations, we have extracted Local Solar Time (LST) and annual variations from the time-series of grids (Calabia and Jin, 2016b). The process consists of removing these parameterized contributions from the main time-expansion PCA components. The parameterizations are based on sinusoidal functions modulated by the extreme ultraviolet (EUV) radiation. A commonly used proxy to represent the thermospheric density variation due to the EUV radiation is the P10.7=0.5 ($F10.7+F10.7_{81\ days}$) composite index from the previous day (e.g., Müller et al., 2009), where F10.7 is the solar radio flux at 10.7 cm (http://omniweb.gsfc.nasa.gov/form/dx1.html). Therefore, the removal procedure has been realized as follows: First, data normalization to common flux has been implemented following the indications in Müller et al. (2009); then a sinusoidal fitting based on Fourier functions has been conducted as done in Jin et al. (2007); and finally a polynomial fitting modulates the flux-dependent amplitude of the functions computed in the previous step. The final equation has the following expression (dimensionless units):

$$G(\chi, P107) = 10^{-15}\cdot 10^{a}\cdot P107^{b}\cdot\left(a0 + \sum_{i=1}^{n}\left[an\cdot cos(n\cdot\chi\cdot w) + bn\cdot sin(n\cdot\chi\cdot w)\right]\right) \quad (8)$$

were *a, b, a0, an, bn* and *w* are the constant and amplitudes, and χ takes different values for each periodic case. For the annual variations, χ is the day of the year (doy) and for the LST variation, χ is the β' angle (angle between the Earth-Sun line and the orbit plane).

3. Results and analysis

In this section, the accuracy of POE-based thermospheric mass densities is investigated, and the responses to the March 2013 geomagnetic storm are analyzed. The purpose of this section is intended to demonstrate that POE-based thermospheric mass densities, inferred from interpolation and numerical differentiation of reduced-dynamic precise orbit velocities, are suitable for monitoring thermosphere mass density variations in both long-term and short-term scales.

3.1. GPS POE-based thermospheric mass densities

GPS POE-based thermospheric mass densities along GRACE's orbital paths are estimated for the period 2011–2016. Two different drag-conditions are given as example in Fig. 1, showing the accelerometer measurements in the satellite body reference system (SBS) together with the GPS POE-based non-gravitational accelerations from 14 February 2011 and 13 April 2012. Note in SBS, the X-axis is the long axis of symmetry of the satellite, pointing in the direction of the microwave horn, the Y-axis is the vertical axis of symmetry, and the Z-axis completes the right-handed coordinate system. In this figure, it can be seen that non-gravitational accelerations in April 2012 were larger than in February 2011. However, the differences between accelerometer measurements and GPS POD-estimates seem not to be dependent on the background density (the uncertainty analysis is presented in the next section). Note that accelerometer measurements have been calibrated using the daily mean averages of POE-based non-gravitational accelerations, so there are no significant differences with respect to daily mean values. Parameterizations for bias calibration employing unitary scale factors are given in Calabia et al. (2015).

In the middle panels of Fig. 1, the Y_{SBS} and Z_{SBS} components show relatively strong short-term variations with respect to accelerometer measurements (note that Y_{SBS} and Z_{SBS} panels are not equally scaled with respect to X_{SBS} panels). For the Y-axis, these variations are mostly related to errors in the horizontal-wind model, and those included by the POD process, e.g., sinusoidal disturbing signal found by Calabia et al. (2015). For the Z-axis, the short-term variations can be mostly attributed to errors in the gravitational and irradiative force-models. A further study on these short-term variations for the Z-axis can be found in Calabia and Jin (2016a). Bottom of Fig. 1 shows the corresponding

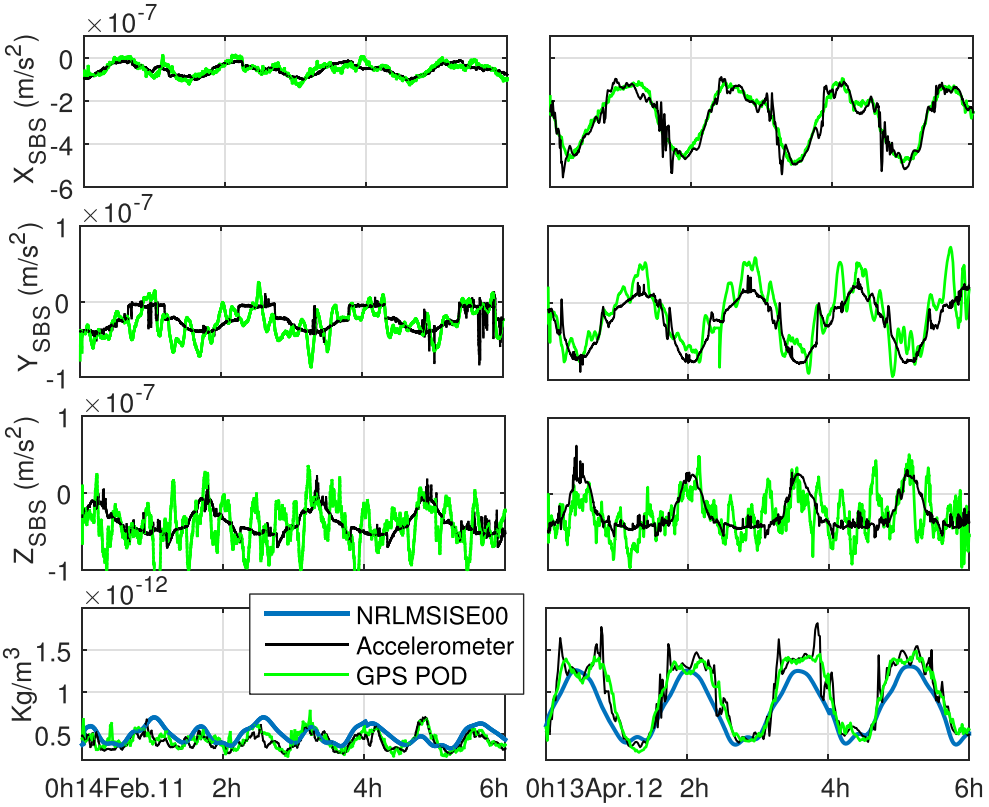

Fig. 1. From top to bottom, non-gravitational accelerations (X, Y, Z)$_{SBS}$ and thermospheric mass densities (normalized to 475 km) along GRACE's orbital path on (left panels) 14 February 2011 and (right panels) 13 April 2012. Accelerometer measurements are plotted in black and the estimations from GPS POE are represented in green. In the bottom panel, the NRLMSISE00 model estimations are shown in blue thick line. (For interpretation of the references to color in this figure legend, the reader is referred to the web version of this article.).

densities inferred from accelerometer measurements and from GPS-POE estimates, together with the NRLMSISE00 empirical model. Note that inferred densities are mostly dependent on the along-track direction. In the bottom panels, the POE-based mass densities show good agreement with the accelerometer-based densities, with a better correlated amplitude and shape than the NRLMSISE00 empirical model. Further analysis on the differences and correlations between estimates are given in the followings sections.

After 9 years of continuous operation, the battery performance of GRACE has obliged to turn off the accelerometers during intermittent periods of approximately one month. In order to fill the data-gaps, we employ thermospheric mass densities inferred from GRACE's POE-based non-gravitational accelerations. For example, Fig. 2 shows the non-gravitational accelerations (X-Y-Z satellite body reference system) inferred from the GPS-POE of GRACE A (GA) and B (GB) satellites on 23 April 2012. During this month, accelerometer measurements are unavailable for both GA and GB satellites. Besides the bias in the Z axis produced by orbiting with different pitch angles (necessary to ensure the line-of-sight orientation between both satellites), there is a clear agreement between both GA and GB satellites. On that day, the along-track acceleration decreased $2{\cdot}10^{-7}$ m/s^2 due to by a G2-level moderate geomagnetic storm. In Fig. 3, the corresponding mass densities are plotted together with those estimated by the NRLMSISE00 empirical model. GRACE's angle β` during this period is ~165° (Sun to ascending leg), so higher values of density correspond to the sunlight side of Earth, and the cusp regions are located in between each day-to-night transition (i.e., in between high-to-low density values). Although the MSIS model is dependent on the geomagnetic Ap index, differences in the diurnal amplitude and mean deviated values can be recognized in Fig. 3. For instance, the empirical model underestimates on 24 April 2012 at 2 h the peak of maximum density anomaly in $1{\cdot}10^{13}$ kg/m^3, and overestimates it over the mean value in about $2{\cdot}10^{13}$ kg/m^3, during 6 hour previous to the event, and about 9 h after the event. In addition, miss-modeled short-term enhancements can be recognized at the beginning of the storm (18–24 h on 23 April 2012, in between each day-to-night orbital transition). It is clear that the MSIS model can

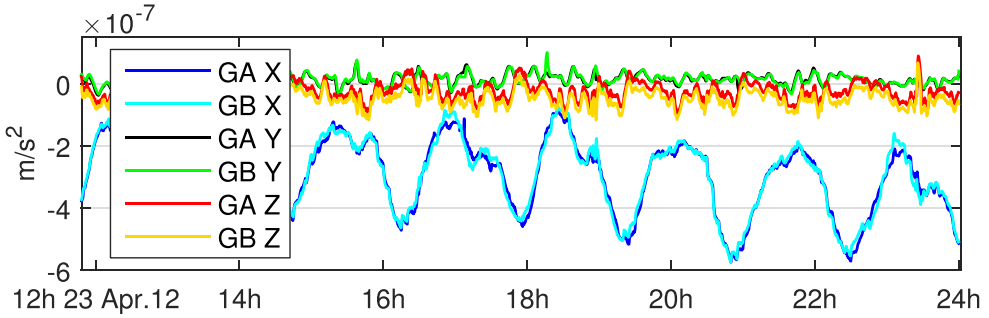

Fig. 2. Non-gravitational accelerations (X-Y-Z satellite body reference system) inferred from the GPS-POE of GRACE-A (GA) and GRACE-B (GB) on 23 April 2012. During this month, accelerometer measurements are unavailable due to instrument power-off.

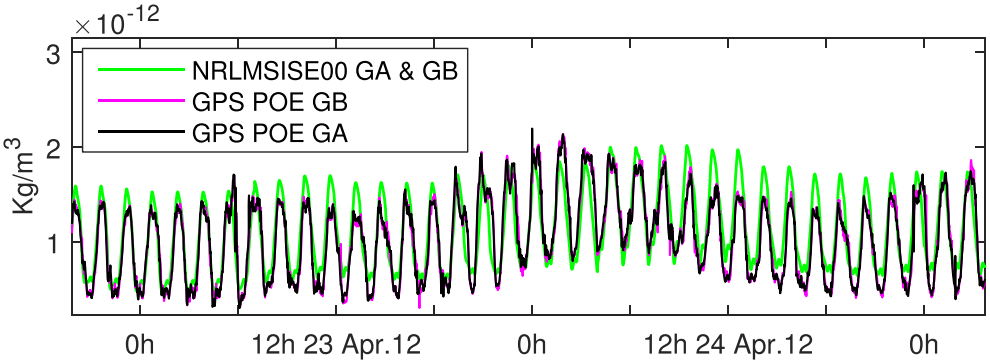

Fig. 3. Thermospheric mass densities along GRACE's orbital path on 23 April 2012. During this month, accelerometer measurements are unavailable due to instrument power-off. The densities estimated from the NRLMSISE00 model are plotted in green, and the results from GRACE GPS-POE are shown in black and magenta colors. (For interpretation of the references to color in this figure legend, the reader is referred to the web version of this article.).

poorly reproduce all the involved density variations due to geomagnetic storms.

3.2. Uncertainty analysis

The analysis presented in this section aims to provide an assessment in space and time for the accuracy of POE-based mass density estimates, as well as the NRLMSISE00 empirical model, using the accurate accelerometer measurements as a reference. Fig. 4 pictures the Pearson's linear correlation coefficients and standard deviations (SD), including fitted trend, for each SBS-axis of daily GPS POD non-gravitational accelerations, with respect to accelerometer measurements. The correlation coefficients for the X $_{SBS}$, Y $_{SBS}$, and Z_{SBS} axes have mean values of 97%, 58%, and 36% respectively. A clear periodicity of 165 day suggests dependence on the LST, increasing the correlation when the satellite's orbit plane is aligned with the Earth-Sun line (i.e., the day-night variation increases the correlation). Fig. 4 (bottom) shows that the SD of the differences between accelerometer measurements and GPS POD-estimates increases its value from 20–30 nm/s^2 in 2011 up to 40–50 nm/s^2 in 2015 (probably related to the orbital decay). A possible correlation with the magnitude of the background density is revised in the followings analysis.

Comparisons for the GPS POD and the NRLMSISE00 estimates with respect to the accelerometer-based densities are shown in Fig. 5, showing from top to bottom the correlation coefficients, the differences

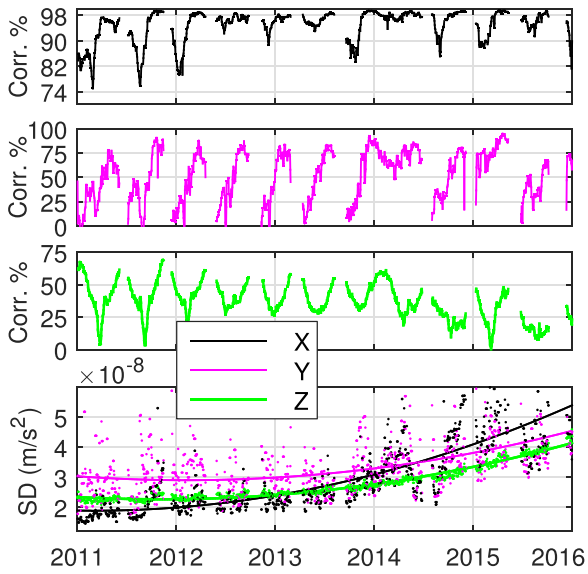

Fig. 4. From top to bottom, correlation coefficients for each axis in the SBS and SD (including fitted trend) of daily GPS POD non-gravitational accelerations with respect to the accelerometer measurements.

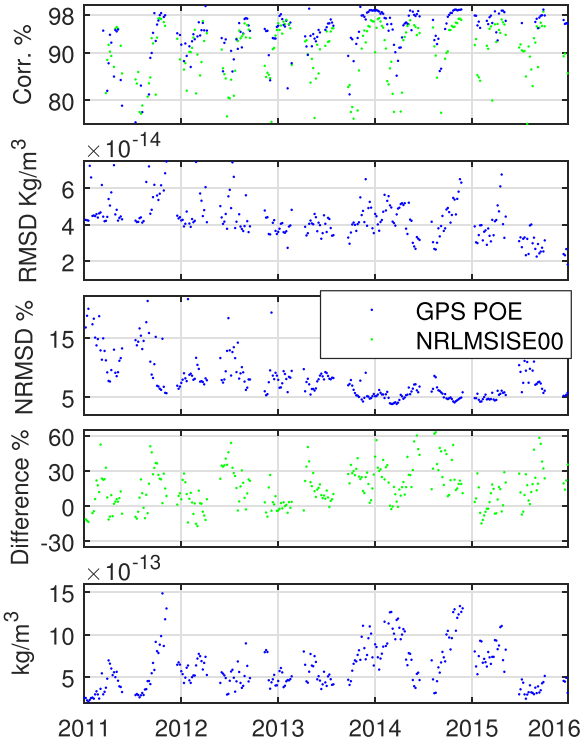

Fig. 5. From top to bottom, correlation coefficients, RMSD, NRMSD, and differences for the GPS POD (blue) and the NRLMSISE00 (green) estimates with respect to the accelerometer-based densities. Bottom panel pictures the mean background density. Each value corresponds to a 5-day mean average along the GRACE's orbital path. (For interpretation of the references to color in this figure legend, the reader is referred to the web version of this article.).

in terms of root-mean-square deviation (RMSD), the normalized RMSD (NRMSD) and direct differences, and the density values along the GRACE's orbital path (time series of 5-day averaged values). In Fig. 5 (top), the GPS POD densities show a clear better correlation than the NRLMSISE00 estimates. In this figure, the above commented periodicity of 165 day (seen in Fig. 4) is also present in both GPS POD and NRLMSISE00 cases (i.e., the day-night variation increases the correlation). Assuming the dependence on this 165-day variation, the correlation of GPS POD densities show most of peak values above 98%, and generally being 5% better that those given by the NRLMSISE00 model. In next panel, the RMSD shows a decreasing trend of $4 \cdot 10^{-14}$ kg/m^3 from 2011 to 2016. In Fig. 5, the corresponding normalized RMSD (NRMSD) pictures a trend from 12% to 5% (following the magnitude of the background density). Lower variations are seen during high-density periods, and higher variations during low-density periods (see bottom panel). In the followings analysis, we will show

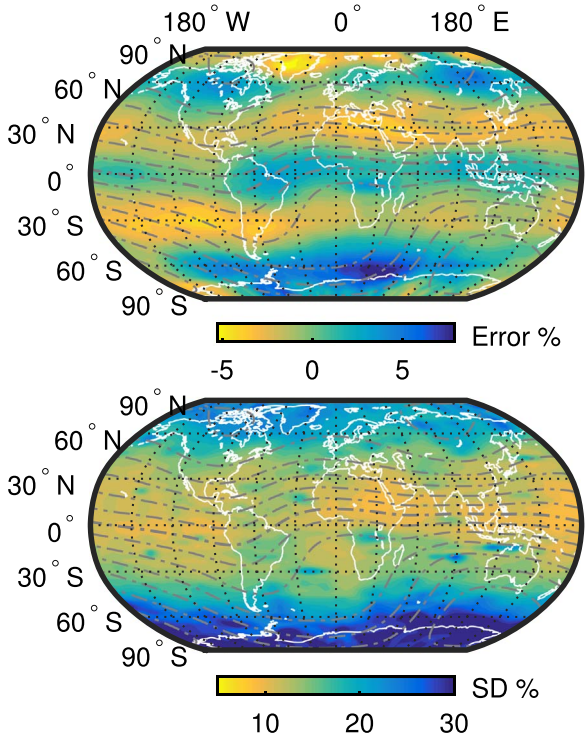

Fig. 6. Mean average (top) and SD (bottom) of relative errors based on the differences between the POE-based and the accelerometer-based thermospheric mass densities, i.e. (POE-ACC)/ACC, inferred from GRACE measurements during 2011-2016. The vertical magnetic field component (Z) is plotted in dash-dot lines.

that the dependence on the background density correlates better when separating ascending from descending orbits. On the other side, the differences for the NRLMSISE00 densities (Fig. 5, fourth panel) show a mean overestimation of 15 ± 18% over the background density.

Fig. 6 shows the mean averages (top) and the SD (bottom) in geographical coordinates, of the relative differences between the POE-based and the ACC-based densities during the period 2011–2016, i.e., (POE-ACC)/ACC. The map of mean averages (Fig. 6, top) shows a mean overestimation by 7% at the equator and the poles, with marked anomalies near the magnetic cusps and clear alignments with the vertical magnetic field component (Z). The middle latitude is underestimated by 5%, following the vertical magnetic field component (Z). The SD map (Fig. 6, bottom) shows a mean value of 15%, with lower values at the equator (7%) and especially higher at the southern pole (up to 30%). A possible role of orbit errors due to geomagnetic activity might produce these marked alignments with geomagnetic equator and poles.

In Fig. 7, the global averaged densities along descending and ascending orbits are plotted for both accelerometer and POE based techniques. The days when accelerometers where powered off are pictured in the bottom time line. The corresponding discontinuities in the accelerometer-based densities can be seen in all the panels of Fig. 7. Taking accelerometer measurements as accurate reference, the relative errors for the GPS POD estimates are shown for both ascending and descending orbits. As expected, the maxima amplitude of the differences reaches up to 10%, mostly during low density periods. During low-density periods, the differences stay below 5% of the background density.

Finally, we employ the PCA to accurately study the differences between the POE-based and the accelerometer-based thermospheric mass densities during the period 2011-2016. The four leading eigenvectors together account for 28% of the total variance and, individually, explain 11%, 8%, 5% and 4% of the total variability. The small percentages of both each pattern and the sum of them indicate that the variability is considerably noisy. The first spatial PCA (Fig. 8, top) shows a clear alignment with the vertical magnetic field component (Z), revealing the role of orbit errors related to geomagnetic activity. Its corresponding time-expansion coefficient is 60% correlated with the background mean density (panel below PCA1). The second PCA component seems to define a mid-latitude underestimation, and overestimation at the equator and polar region, with a northern cusp-

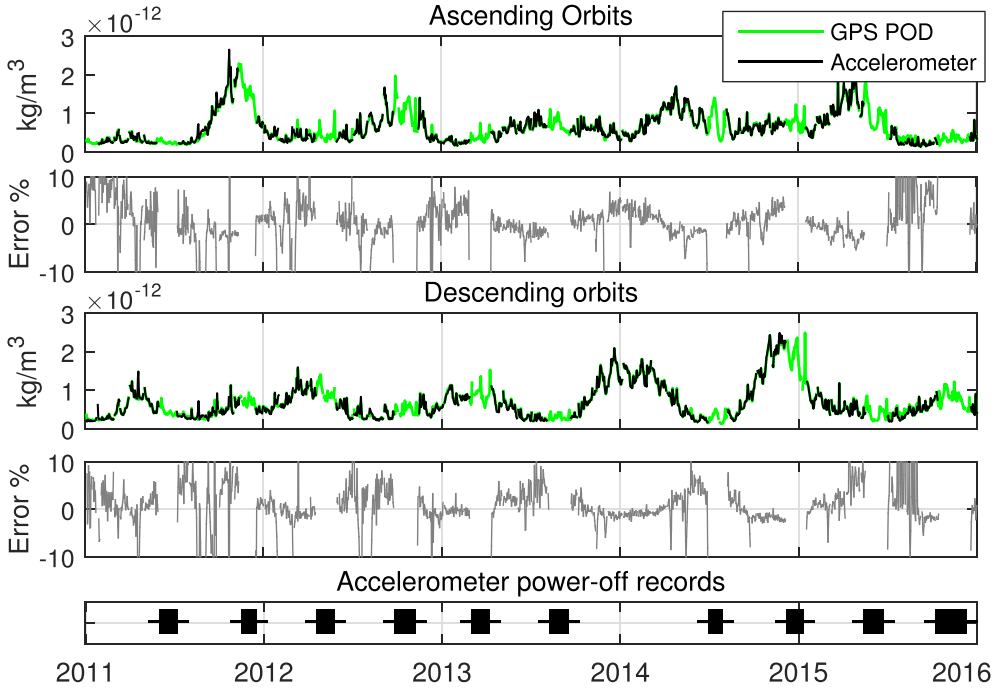

Fig. 7. Global daily averaged densities and differences of relative errors between the POE-based and the accelerometer-based densities (2011–2016), i.e. (POE-ACC)/ACC, separated in ascending orbits (top panels) and descending orbits (bottom panels). Accelerometer-based densities are plotted in black and GRACE GPS-POE estimates are plotted in green. Bottom time-line shows the days when accelerometer measurements were turned off due to power requirements. (For interpretation of the references to color in this figure legend, the reader is referred to the web version of this article.).

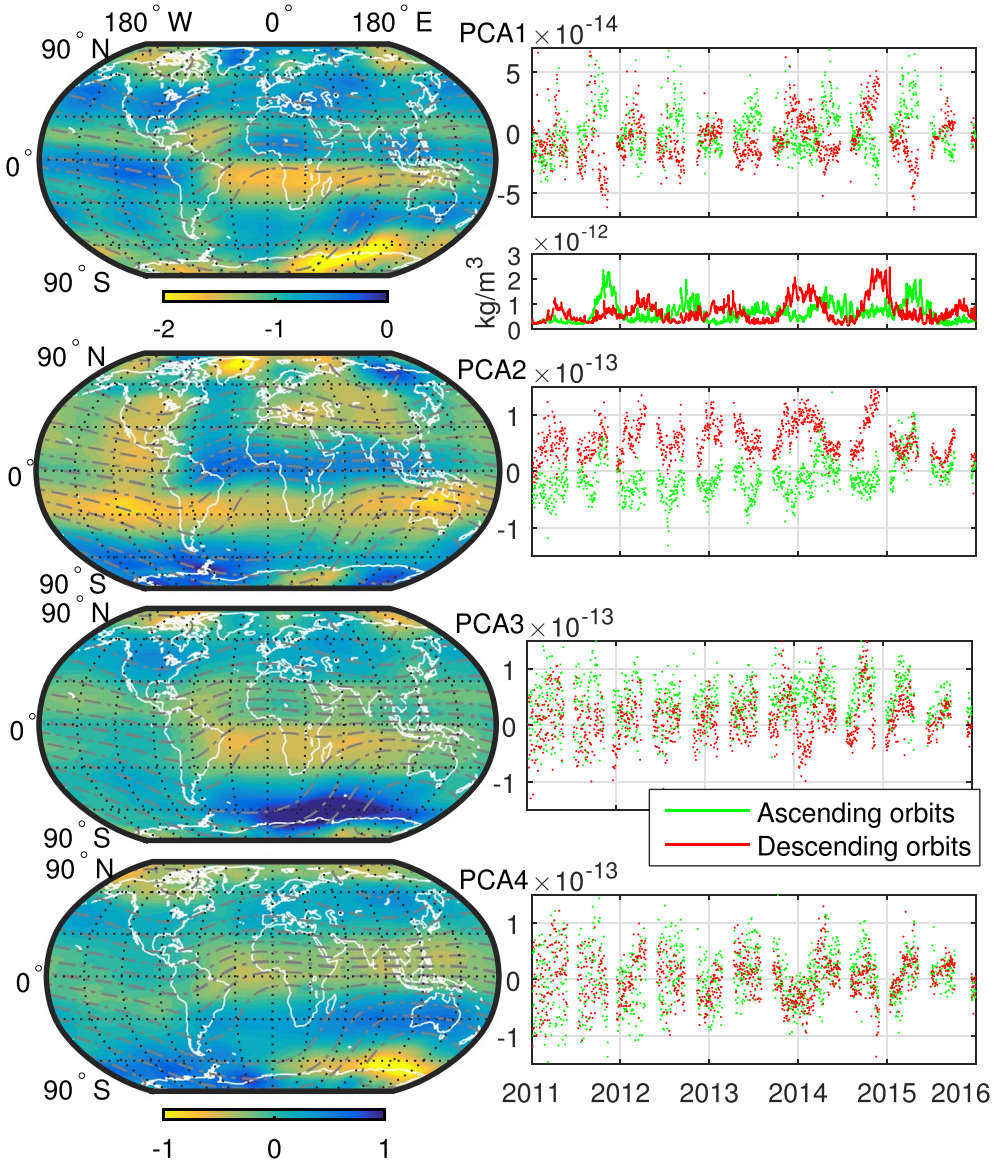

Fig. 8. Four main PCA components for the variability of the differences between the POE-based and the accelerometer thermospheric mass densities (2011 to 2016). Values are dimensionless. From top to bottom, each component explains the 11%, 8%, 5% and 4% of the total variability. The global averaged densities from Fig. 7 are included below the first PCA. Ascending orbits are represented in green and descending orbits in red. The vertical magnetic field component (Z) is plotted in dash-dot lines. (For interpretation of the references to color in this figure legend, the reader is referred to the web version of this article.).

related anomaly. It can be seen for this component a clear opposite behavior between ascending and descending orbits. The corresponding time-expansion coefficients is centered at $5{\cdot}10^{-14}$, being negative for ascending orbits and positive for descending orbits. Third and fourth PCA components seem to be defined as a time series of southern-cusp variations. Both PCA3 and PCA4 show correlation all along the period 2011–2016.

3.3. Thermospheric mass density variations during the March 2013 geomagnetic storm

On 15 March 2013, the Sun flared an Earth-directed coronal mass ejection (CME) during a period of low solar-flux circumstances (F10.7 ≈120 s.f.u.). At that moment, the solar wind increased up to 700 km/s, along with a southwards B_z component of the interplanetary magnetic field (IMF). On 17 March 2013, the halo CME arrived at Earth and produced a moderate G2-level geomagnetic storm. Consequently, the energetic solar wind plasma with the favorable IMF disposition produced thermospheric Joule heating and particle precipitation along the Earth's magnetic field lines (e.g., Jin et al., 2008). In the upper atmosphere, the density is too low for molecular interactions, and the dynamics acted through the collisions between the ionospheric plasma and the neutrals, creating anomalous variations in the air mass density distribution. During this period, the GRACE satellites were approximately located at 0 h LST and the corresponding +12 h for their complementary descending orbital leg. Since accelerometer measurements are not available during this storm (due to instrument power-off), we employ GPS POE-based thermospheric mass densities to characterize the anomalous variations of density. In addition, since the thermosphere response to geomagnetic activity can be investigated in relation with space weather and geomagnetic indices, these have been downloaded from the website of the Low Resolution OMNI (LRO) data set of NASA (http://omniweb.gsfc.nasa.gov/form/dx1.html), and from the International Service of Geomagnetic Indices (ISGI) website (http://isgi.unistra.fr/data_download.php). We also have computed the merging electric field E_m following the indications in Liu et al. (2010).

Previous to study short-term variations, we have extracted LST and

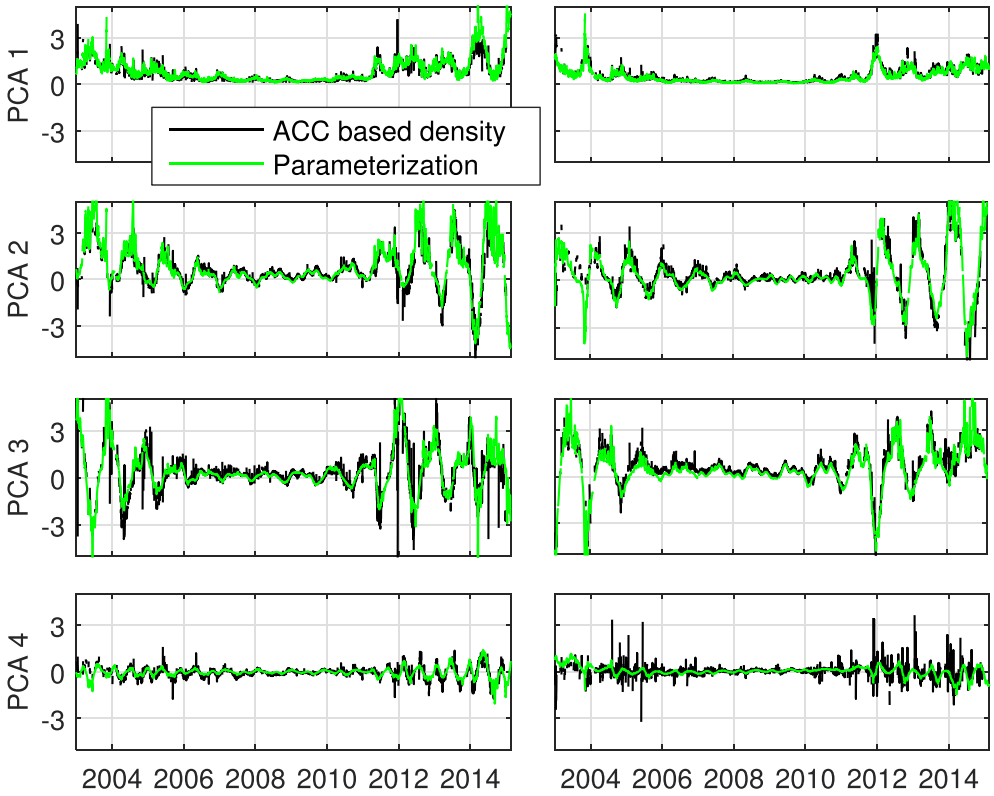

Fig. 9. Main PCA coefficients (black) and corresponding parameterizations (green) in function of P10.7, LST, and annual variations. 12 year of accelerometer-based densities (2003–2015). Descending orbits on the left panels and ascending orbits in the right panels. Values are dimensionless. (For interpretation of the references to color in this figure legend, the reader is referred to the web version of this article.).

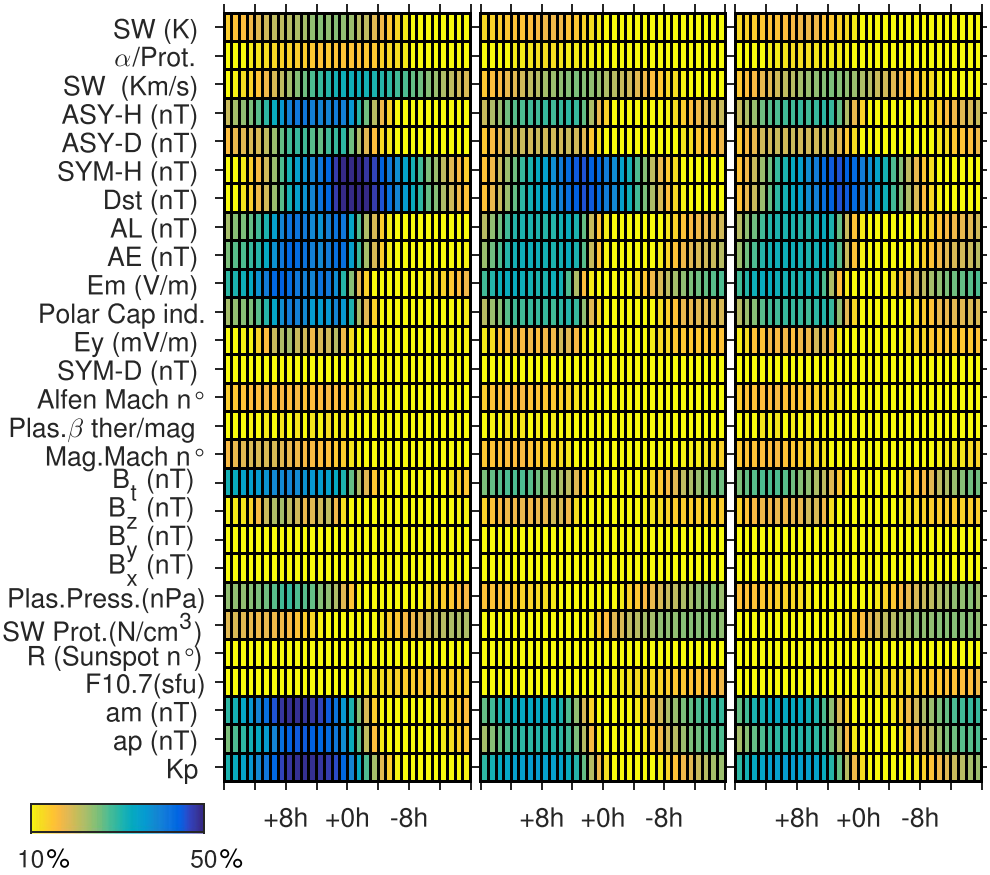

Fig. 10. Correlation coefficients versus delay-times for space weather and geomagnetic indices with respect to short-term density variations during 2011–2016. Values for (left) northern, (middle) equatorial, and (right) southern regions.

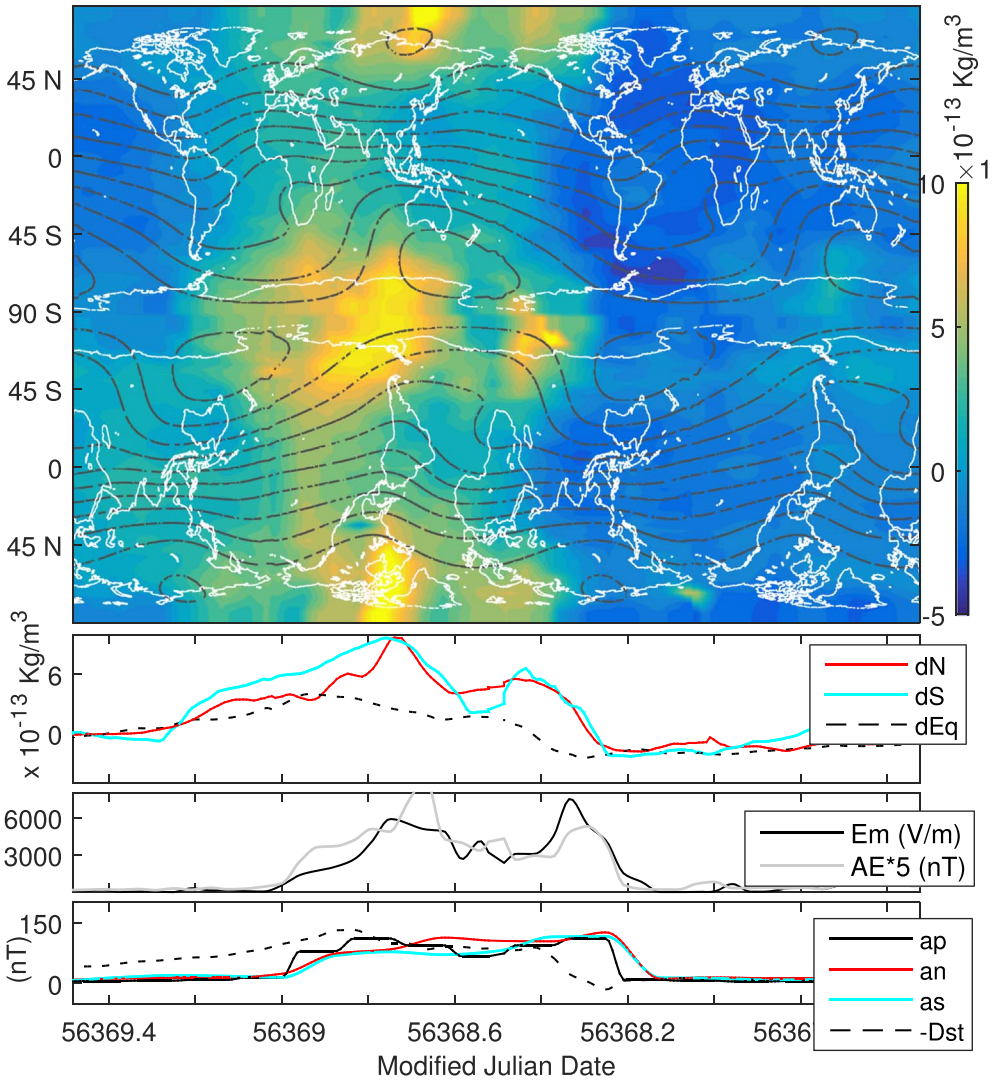

Fig. 11. Short-term thermospheric density variations inferred from GRACE GPS-POE and its profiles at equator (*dEq*) and poles (*dN*, *dS*), plotted together with E_m, *AE*, *ap*, *an*, and *as*, for the moderate G2-level geomagnetic storm of 16-17 March 2013 (from right to left and from bottom to top: 16/Mar./2013 12^h 36^m to 18/Mar/2013 11^h 35^m). GRACE's angle β` during this period is 173° (Sun to ascending leg). Accelerometer-based densities are not available due to instrument power-off during this month. The vertical magnetic field component (Z) is plotted in dash-dot lines.

Table 1
Maximum values and respective delay-times for the correlation coefficients between space weather and geomagnetic indices and short-term density variations during 2011–2016. Values for the northern, equatorial, and southern regions.

	North		Equator		South	
	max (%)	delay (h)	max (%)	delay (h)	max (%)	delay (h)
Kp	49	6	36	9	40	3
ap (nT)	45	6	31	7	36	3
am (nT)	49	7	34	9	41	4
Bz (nT)	23	9	20	7	22	3
Bt (nT)	40	8	29	12	30	8
Ey (mV/m)	24	8	20	6	24	2
PC ind.	41	8	31	5	37	1
Em (V/m)	45	9	33	13	38	3
AE ind.(nT)	44	8	34	5	41	1
AL ind. (nT)	42	8	33	5	40	1
Dst (nT)	52	0	46	3	43	0
SYM-H (nT)	51	0	46	3	43	0
ASY-D (nT)	30	1	21	5	27	1
ASY-H (nT)	41	6	30	5	36	1
SW (Km/s)	33	0	26	4	29	0
SW Temp.(K)	25	4	18	8	23	2

annual variations from the time-series of grids (Calabia and Jin, 2016b). Fig. 9 shows the main time-expansion PCA components and the parameterizations in terms of P10.7, LST and annual variations for 12 year (2003-2015) of accelerometer-based densities. The four leading PCA components together account for 99.8% of the total variance and, individually, explain 92%, 3.5%, 3%, and 1.3% of the total variability. The high percentage for the first PCA component is due to the main dependence on the EUV radiation, and the high percentage for the sum of four leading PCA components indicates low noise with few marked patterns of variability. The correlation coefficients for the parameterized time series are respectively 96%, 93%, 90%, and 83%, being more than acceptable for the purpose of this study.

After reconstructing the grid-time-series from removing the parameterized time-expansion coefficients, three density profiles (North, South, and Equator) have been extracted and investigated in relation to the space weather and geomagnetic indices. Correlation coefficients have been calculated for hourly delay-times ranging from ± 16 h for the northern (*dN*), southern (*dS*), and equatorial regions (*dEq*). The density profiles for each region correspond to an averaged density of 30° in latitude (see example in Fig. 11). Fig. 10 shows the correlation coefficients between the space weather and geomagnetic indices and the short-term density variations (free from LST and annual varia-

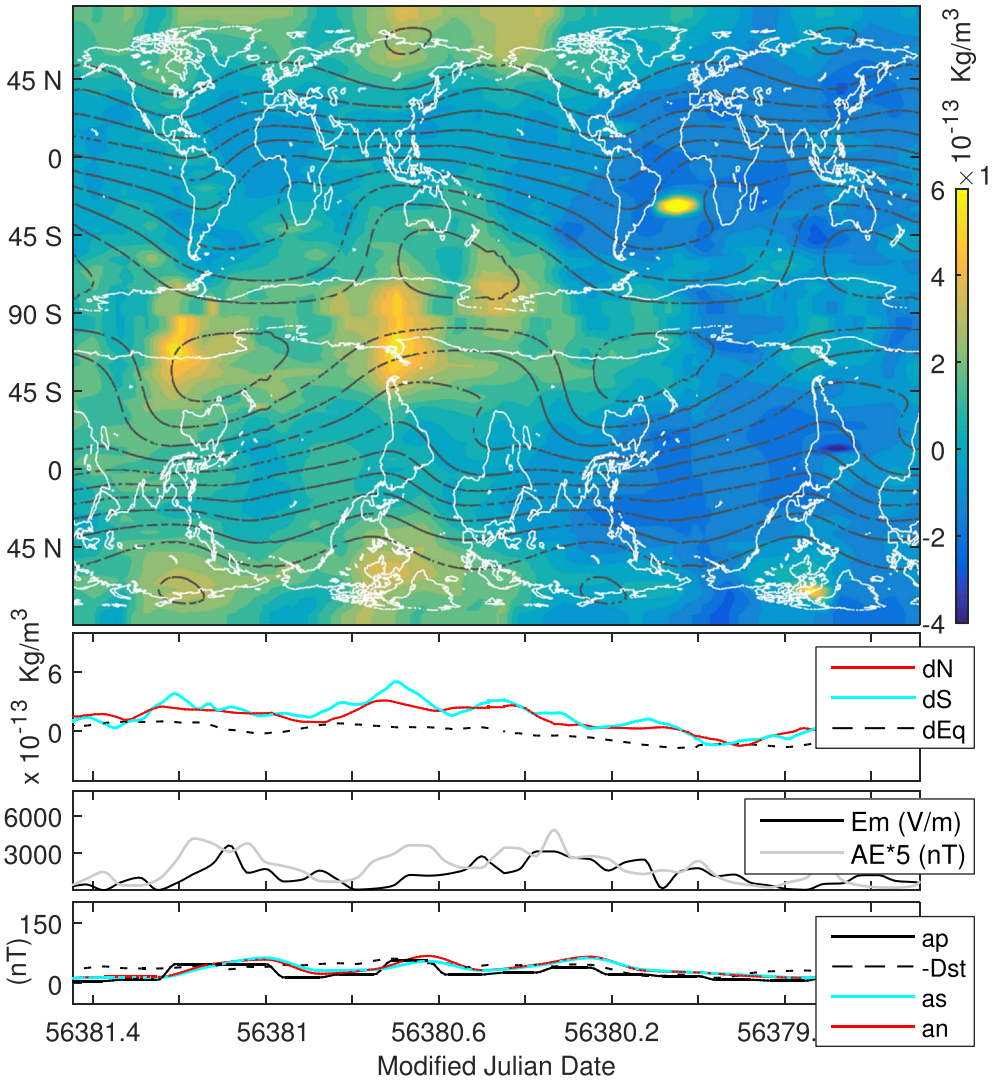

Fig. 12. Short-term thermospheric density variations inferred from GRACE GPS-POE and its profiles at equator (*dEq*) and poles (*dN*, *dS*), plotted together with E_m, *AE*, *ap*, *an*, and *as*, for the minor G1-level geomagnetic storm of 28-29 March 2013 (from right to left and from bottom to top: 28/Mar/2013 11^h 42^m to 30/Mar/2013 10^h 41^m). GRACE's angle β` during this period is 186° (Sun to ascending leg). Accelerometer-based densities are not available due to instrument power-off during this month. The vertical magnetic field component (Z) is plotted in dash-dot gray lines.

tions). Detailed description for each index can be found in the OMNI and ISGI websites. Maximum correlations and their respective delay-times for some selected indices are given in Table 1. Best correlations are found when employing the k-derived planetary indices (*Kp, ap, am*), the interplanetary total magnetic field B_T, the Polar Cap index horizontal component disturbances *PC*, the E_m , the auroral index horizontal component disturbances (*AE*, *AL*), the equatorial index horizontal component disturbances *Dst*, the longitudinally asymmetric and symmetric horizontal component disturbances (*SYM-H, ASY-D, ASY-H*), and the solar wind (SW) velocity and temperature (note that *SYM-H* is essentially the same as the *Dst* index with a different time resolution). From Table 1, the highest correlation is achieved when employing the *Dst* index, being about 45% for Equator and Southern regions, and 52% for the Northern region. The corresponding time-delays for these maxima are null for high latitudes and about 3 h for low latitudes. K-derived planetary indices (*Kp, ap, am*) show better represent the high-latitude than the low-latitude density variations in about 10%, and with about 3, 6 and 9 h delay for the Southern, Northern, and Equatorial regions respectively.

Fig. 11 shows the short-term thermospheric density variations (free from Local Time and annual variations) inferred from GRACE GPS-POE during the moderate G2-level geomagnetic storm of 16-17 March 2013. In this figure, time evolution is defined from right to left (Earth rotation with respect to GRACE's orbital plane), and from bottom to top (satellite's along-track direction). Bottom panels of Fig. 11 show the corresponding *dN*, *dS* and *dEq* profiles of density, and the *AE*, E_m, *Dst*, *ap*, *as* and *an* indices. Note that *an* (North) and *as* (South) correspond to the hemispheric indices employed to obtain the *am* index (*am* = (*an* + *as*) / 2). Although Fig. 10 and Table 1 show that density variations better correlate with *Dst* and k-derived geomagnetic indices, Fig. 11 shows that high-latitude density (*dN* and *dS*) have better agreement with *AE* and E_m, . For instance, the two peaks of density seen in *dN* and *dS* at 56368.4 MJD and 56368.7 MJD have better agreement with *AE* and E_m (3 h delay). On the other hand, *an*, *as*, and *ap* seem to deficiently agree with these two peaks. As for the low latitude variations, the *Dst* index shows better agreement with the *dEq* profile (3 h delay). Low-latitude variations are well represented with the equatorial *Dst* index (3h delay).

On 26 March 2013, a new sunspot was detected into the eastern solar limb, and a minor G1-level geomagnetic storm was noticed on 29 March 2013. Fig. 12 shows the short-term density variations due to this minor geomagnetic storm. Once again, a better agreement is found for *AE* and E_m when comparing with high-latitude variations (*dN* and *dS*), and for *Dst* for the low-latitude variations (*dEq*).

4. Conclusion

In this paper, thermospheric mass densities are estimated from interpolated and numerically differentiated GRACE's precise orbit velocities. The derived data can be used to fill the accelerometer data-gaps due to instrument malfunction or power-off. Our POE-based density estimates show good agreement with the accelerometer-based densities, and a better estimation than the NRLMSISE00 empirical model. The uncertainty analysis of GRACE GPS-POE inferred thermospheric densities during these periods shows low relative error (< 10%) with respect to the accurate accelerometer measurements. The uncertainty analysis using the PCA shows small contributions of the 4 main patterns (11%, 8%, 5% and 4%) and the sum of them (28%), indicating that the error is considerably noisy.

Some guidelines are addressed for the improvement of accuracy in the POD, showing errors aligned to the geomagnetic equator and poles. Furthermore, detailed variations during the 2013 geomagnetic storm are obtained from short-term GRACE GPS-POE inferred thermospheric densities (free from LST and annual fluctuations). Although our correlation study has shown that short-term density variations better correlate with the *Dst* and k-derived geomagnetic indices, the auroral electroject activity index *AE* as well as the merging electric field E_m pictures better agreement for the March 2013 geomagnetic storm at high latitudes for this period. On the other side, low-latitude variations are better represented with the equatorial *Dst* index.

The results are intended to promote the improvement of the current force-models used in POD with the analysis of accurate GPS-POE and accelerometer measurements. Our results can picture even variations from minor geomagnetic storms (e.g., 28-29 March 2013, Fig. 12), but further research is required to compare the numerical integration method with the POD strategies (e.g. Kuang et al., 2014; van den IJssel and Visser, 2010) for estimation of non-gravitational forces from GPS data. Nevertheless, thermospheric mass density estimates trough numerical differentiation of reduced-dynamic precise orbit velocities is a new and promising technique, which can be used as alternative to the POD strategy. With the increasing number of LEO satellites being equipped with a high-precision GPS receivers and more enhanced data processing and orbit determination strategies, we believe that GPS-POE can be used to investigate the geophysical processes in the ionosphere-thermosphere system. We expect soon to provide accurate POE-based non-gravitational accelerations and thermospheric mass density estimates from other low-orbit satellite missions.

Acknowledgments

This work was supported by the National Keystone Basic Research Program (MOST 973) (Grant No. 2012CB72000), National Natural Science Foundation of China (NSFC) Project (Grant No. 11573052) and Shanghai Science and Technology Commission Project (Grant No. 12DZ2273300). Great appreciation is extended to ISDC, ISGI, and NASA for providing the data access. There is no conflict of interest regarding the publication of this paper. Thanks to the editor and two reviewers for their constructive comments and helpful suggestions on an earlier version of the manuscript.

References

Bertiger, W., Bar-Sever, Y., Bettadpur, S., Dunn, C., Haines, B., Kruizinga, G., Kuang, D., Nandi, S., Romans, L., Watkins, M., Wu, S., 2002. GRACE: millimeters and microns in orbit. In: Proceedings of ION GPS 2002, Portland, OR, September 24–27, 2002, pp. 2022–2029.

Bettadpur, S., 2012. Product Specification Document. Technical Report CSR-GR-03-02, Center for Space Research, The University of Texas at Austin, ⟨ftp://podaac.jpl.nasa.gov/allData/grace/docs/ProdSpecDoc_v4.6.pdf⟩).

Bezděk, A., 2010. Calibration of accelerometers aboard GRACE satellites by comparison with POD-based nongravitational accelerations. J. Geodyn. 50 (5), 410–423. http://dx.doi.org/10.1016/j.jog.2010.05.001.

Bhanderi, D., 2005. Spacecraft Attitude Determination with Earth Albedo Corrected Sun Sensor Measurements (Dissertation). Aalborg University, Denmark.

Bjornsson, H., Venegas, S.A., 1997. A Manual for EOF and SVD Analyses of Climatic Data. CCGCR Report No. 97-1. MCGill University, Montréal, Québec, 52.

Bruinsma, S., Tamagnan, D., Biancale, R., 2004. Atmospheric densities from CHAMP/STAR accelerometer observations. Planet. Space. Sci. 52, 297–312. http://dx.doi.org/10.1016/j.pss.2003.11.004.

Bruinsma, S., Forbes, J.M., Nerem, R.S., Zhang, X., 2006. Thermosphere density response to the 20–21 November 2003 solar and geomagnetic storm from CHAMP and GRACE accelerometer data. J. Geophys. Res. 111, A06303.

Calabia, A., Jin, S.G., 2015. GPS-based non-gravitational accelerations and accelerometer calibration. In: Jin, S. (Ed.), Satellite positioning: methods, models and applications. InTech-Publisher, Rijeka, Croatia, 47–72.

Calabia, A., Jin, S.G., 2016a. Assessment of conservative force models from GRACE accelerometers and precise orbit determination. Aerosp. Sci. Technol. 49, 80–87. http://dx.doi.org/10.1016/j.ast.2015.11.034.

Calabia, A., Jin, S.G., 2016b. New modes and mechanisms of thermospheric mass density variations from GRACE accelerometers. J. Geophys. Res. Space. Phys.. http://dx.doi.org/10.1002/ 2016JA022594.

Calabia, A., Jin, S.G., Tenzer, R., 2015. A new GPS-based calibration of GRACE accelerometers using the arc-to-chord threshold uncovered sinusoidal disturbing signal. Aerosp. Sci. Technol. 45, 265–271. http://dx.doi.org/10.1016/j.ast.2015.05.013.

Doornbos, E., 2011. Thermospheric Density and Wind Determination from Satellite Dynamics. Dissertation, TU Delft.

Doornbos, E., Visser, P., Koppenwallner G, and Fritsche S, 2014. GOCE+ theme 3: Air density and wind retrieval using GOCE data. Algorithm Theoretical Basis Document, Tech. Rep. ESA AO/1-6367/10/NL/AF, TU Delft, Netherlands.

Drob, D.P., et al., 2008. An empirical model of the Earth's horizontal wind fields: HWM07. J. Geophys. Res. 113, A12304. http://dx.doi.org/10.1029/2008JA013668.

van den IJssel, J., Visser, P., 2007. Performance of GPS-based accelerometry: CHAMP and GRACE. Adv. Space Res. 39, 1597–1603. http://dx.doi.org/10.1016/j.asr.2006.12.027.

van den IJssel, J., Visser, P., 2010. Performance of GPS-based accelerometer: a simulation experiment. Adv. Space Res. 45, 225–238. http://dx.doi.org/10.1016/j.asr.2009.09.012.

Jin, S.G., Park, J.U., Cho, J.H., Park, P.H., 2007. Seasonal variability of GPS-derived zenith tropospheric delay (1994–2006) and climate implications. J. Geophys. Res. 112, D09110. http://dx.doi.org/10.1029/2006JD007772.

Jin, S.G., Luo, O.F., Park, P.H., 2008. GPS observations of the ionospheric F2-layer behavior during the 20th November 2003 geomagnetic storm over South Korea. J. Geodesy 82 (12), 883–892. http://dx.doi.org/10.1007/s00190-008-0217-x.

Jin, S.G., van Dam, T., Wdowinski, S., 2013. Observing and understanding the earth system variations from space geodesy. J. Geodyn. 72, 1–10. http://dx.doi.org/10.1016/j.jog.2013.08.001.

Knocke, P., Ries, J., 1987. Earth Radiation Pressure Effects on Satellites. Center for Space Research, Technical Memorandum, CSR-TM-87-01. The University of Texas at Austin.

Kuang, D., Desai, S., Sibthorpe, A., Pi, X., 2014. Measuring atmospheric density using GPS–LEO tracking data. Adv. Space Res. 53 (2), 243–256. http://dx.doi.org/10.1016/j.asr.2013.11.022.

Liu, H., Lühr, H., 2005. Strong disturbance of the upper thermospheric density due to magnetic storms: CHAMP observation. J. Geophys. Res. 110, A09S29.

Liu, R., Lühr, H., Doornbos, E., Ma, S.-Y., 2010. Thermospheric mass density variations during geomagnetic storms and a prediction model based on the merging electric field. Ann. Geophys. 28, 1633–1645.

Liu, R., Ma, S.-Y., Lühr, H., 2011. Predicting storm-time thermospheric mass density variations at CHAMP and GRACE altitudes. Ann. Geophys. 29, 443–453.

Lu, G., Hagan, M.E., Häusler, K., Doornbos, E., Bruinsma, S., Anderson, B.J., Korth, H., 2014. Global ionospheric and thermospheric response to the 5 April 2010 geomagnetic storm: An integrated data-model investigation. J. Geophys. Res. Space Phys. 119, 10/358–10/375. http://dx.doi.org/10.1002/2014JA020555.

Luthcke, S.B., Marshall, J.A., Rowton, S.C., Rachlin, K.E., Cox, C.M., Williamson, R.G., 1997. Enhanced radiative force modeling of the tracking and data relay satellites. J. Astronaut. Sci. 45 (3), 349–370.

Matsuo, T., Forbes, J.M., 2010. Principal modes of thermospheric density variability: Empirical orthogonal function analysis of CHAMP 2001–2008 data. J. Geophys. Res. 115, A07309. http://dx.doi.org/10.1029/2009JA015109.

McLaughlin, C.A., Lechtenberg, T., Fattig, E., Mysore Krishna, D., 2013. Estimating density using precision satellite orbits from multiple satellites. J. Astronaut. Sci. 59 (1–2), 84–100. http://dx.doi.org/10.1007/s40295-013-0007-4.

Mehta, P.M., McLaughlin, C.A., Sutton, E.K., 2013. Drag coefficient modeling for grace using Direct Simulation Monte Carlo. Adv. Space Res. 52, 2035–2051. http://dx.doi.org/10.1016/j.asr.2013.08.033.

Mehta, P.M., Walker, A., McLaughlin, C.A., Koller, J., 2014. Comparing physical drag coefficients computed using different gas–surface interaction models. J. Spacecr. Rockets 51 (3), 873–883. http://dx.doi.org/10.2514/1.A32566.

Montenbruck, O., Gill, E., 2013. Satellite Orbits: Models, Methods and Applications. Springer, Berlin.

Müller, S., Lühr, H., Rentz, S., 2009. Solar and geomagnetic forcing of the low latitude thermospheric mass density as observed by CHAMP. Ann. Geophys. 27, 2087–2099.

Picone, J.M., Hedin, A.E., Drob, D.P., Aikin, A.C., 2002. NRLMSISE-00 empirical model of the atmosphere: statistical comparisons and scientific issues. J. Geophys. Res. 107 (A12), 1468. http://dx.doi.org/10.1029/2002JA009430.

Priester, W., Roemer, M., Volland, H., 1967. The physical behavior of the upper atmosphere deduced from satellite drag data. Space Sci. Rev. 6, 707–780. http://dx.doi.org/10.1186/BF03351782.

Qian, L., Solomon, S.C., 2012. Thermospheric density: an overview of temporal and spatial variations. Space Sci. Rev. 168, 147–173. http://dx.doi.org/10.1007/s11214-011-9810-z.
Rentz, S., Lühr, H., 2008. Climatology of the cusp-related thermospheric mass density anomaly, as derived from CHAMP observations. Ann. Geophys. 26, 2807–2823.
Ridley, A.J., Deng, Y., Toth, G., 2006. The global ionosphere–thermosphere model. J. Atmos. Sol-Terr. Phys. 68 (8), 839–864.
Siemes, C., Teixeira da Encarnação, J., Doornbos, E., et al., 2016. Swarm accelerometer data processing from raw accelerations to thermospheric neutral densities. Earth Planet Sp. 68, 92. http://dx.doi.org/10.1186/s40623-016-0474-5.
Sutton, E.K., 2008. Effects of Solar Disturbances on the Thermosphere Densities and Winds from CHAMP and GRACE Satellite Accelerometer Data. Dissertation. University of Colorado.
Sutton, E.K., Forbes, J.M., Nerem, R.S., 2005. Global thermospheric neutral density and wind response to the severe 2003 geomagnetic storms from CHAMP accelerometer data. J. Geophys. Res. 110, A09S40.
Sutton, E.K., Forbes, J.M., Knipp, D.J., 2009. Rapid response of the thermosphere to variations in Joule heating. J. Geophys. Res. 114, A04319.
Tapley, B.D., Bettadpur, S., Watkins, M., Reigber, C., 2004. The gravity recovery and climate experiment: Mission overview and early results. Geophys. Res. Lett. 31, L09607. http://dx.doi.org/10.1029/2004GL019920.
Taylor, F.W., 2005. Elementary Climate Physics. U Press, Oxford.
van den IJssel, J., 2014. GPS-Based Precise Orbit Determination and Accelerometry for low flying satellites, Dissertation, TU Delft.
Wright, J.R., 2003. Real-time estimation of local atmospheric density. Adv. Astronaut. Sci. 114, 927–950, AAS 03-164.
Wu, S.C., Yunck, T.P., Thornton, C.L., 1991. Reduced-dynamic technique for precise orbit determination of low earth satellites. J. Guid. Control Dyn. 14 (1), 24–30. http://dx.doi.org/10.2514/3.20600.